Supporting Information

Aerobic homocoupling of arylboronic acids using Cu-doped amorphous zirconia: Impact of catalyst amorphousness on reaction efficiency

Masaru Kondo*[a], Tatsuya Joutsuka*[b], Yamato Mori[c], Masahiko Nishijima[d], Tetsuo Honma[e], Akira Miura[c], Shohei Tada*[c]

[a] *School of Pharmaceutical Sciences, University of Shizuoka, Shizuoka, Shizuoka 422-8526, Japan*
[b] *Department of Materials Science and Engineering, Ehime University, 3 Bunkyo-cho, Matsuyama, Ehime 790-8577, Japan*
[c] *Division of Applied Chemistry, Hokkaido University, N13 W8, Kita-ku, Sapporo, Hokkaido 060-8628, Japan*
[d] *Flexible 3D System Integration Lab, SANKEN, Osaka University, Mihogaoka, Ibaraki-shi, Osaka 567-0047, Japan*
[e] *Japan Synchrotron Radiation Research Institute, Hyogo 679-5198, Japan*

Correspondence: mkondo@u-shizuoka-ken.ac.jp
joutsuka.tatsuya.zk@ehime-u.ac.jp
shohei.tada.st@eng.hokudai.ac.jp

CONTENTS:

Reaction test

Each test-tube was charged with *p*-tolylboronic acid **1a** (0.4 mmol, 54.4 mg) and the catalyst (0.04 mmol Cu) in 1 mL MeOH. The resulting solution was stirred at 50 °C in air. After 16 h, the organic layer was separated with the Cu catalyst and concentrated under reduced pressure. The residue was purified by silica gel column chromatography to obtain the pure product **2a**.

Characterization of Compounds

^{1}H-, ^{13}C-, and ^{19}F-NMR spectra were recorded with a Bruker AVANCE III (^{1}H-NMR 400 MHz, ^{13}C-NMR 100 MHz, and ^{19}F-NMR 376 MHz). ^{1}H-NMR spectra are reported as follows: chemical shift in ppm relative to the chemical shift of $CHCl_3$ at 7.26 ppm, integration, multiplicities (s = singlet, d = doublet, t = triple, m = multiplet), and coupling constants (Hz). ^{13}C-NMR spectra reported in ppm relative to the central line of triplet for $CDCl_3$ at 77 ppm. ^{19}F-NMR spectra were reported in ppm relative to the resonance of CF_3COOH (–76.55 ppm). Column chromatography on SiO_2 was performed with Kanto Silica Gel 60 (40-100 μm). Commercially available organic and inorganic compounds were used without further purification.

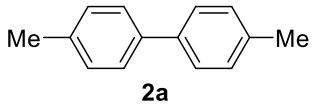

2a

2a: 24.2 mg, 66% yield, white solid; ^{1}H-NMR (400 MHz, $CDCl_3$) δ 7.50 (d, J = 8.0 Hz, 4H), 7.26 (d, J = 8.0 Hz, 4H), 2.41 (s, 6H); ^{13}C-NMR (100 MHz, $CDCl_3$) δ 138.3, 136.7, 129.4, 126.8, 21.0.

^{1}H and ^{13}C NMR charts were consistent with previously reported data.[1]

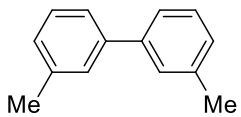

2b

2b: 20.5 mg, 56% yield, colorless oil; ^{1}H-NMR (400 MHz, $CDCl_3$) δ 7.40-7.38 (m, 4H), 7.32 (dd, J = 7.2 Hz, 7.2 Hz, 2H), 7.16 (d, J = 7.2 Hz, 2H), 2.42 (s, 6H); ^{13}C-NMR (100 MHz, $CDCl_3$) δ 141.3, 138.2, 128.6, 128.0, 127.9, 124.3, 21.5.

^{1}H and ^{13}C NMR charts were consistent with previously reported data.[2]

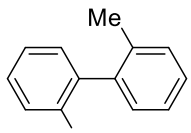

2c

2c: 17.0 mg, 47% yield, colorless oil; ^{1}H-NMR (400 MHz, $CDCl_3$) δ 7.33-7.27 (m, 6H), 7.18-7.16 (m, 2H), 2.12 (s, 6H); ^{13}C-NMR (100 MHz, $CDCl_3$) δ 141.6, 135.8, 129.8, 129.3, 127.1, 125.5, 19.8.

^{1}H and ^{13}C NMR charts were consistent with previously reported data.[1]

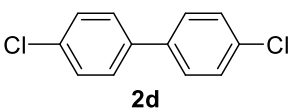

2d

2d: 27.0 mg, 61% yield, white solid; ^{1}H-NMR (400 MHz, $CDCl_3$) δ 7.48 (d, J = 8.8 Hz, 4H), 7.41 (d, J = 8.8 Hz, 4H); ^{13}C-NMR (100 MHz, $CDCl_3$) δ 138.4, 133.7, 129.0, 128.2.

^{1}H and ^{13}C NMR charts were consistent with previously reported data.[3]

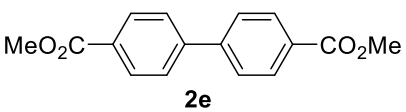

2e

2e: 24.4 mg, 45% yield, white solid; ^{1}H-NMR (400 MHz, $CDCl_3$) δ 8.12 (d, J = 8.8 Hz, 4H), 7.68 (d, J = 8.8 Hz, 4H), 3.95 (s, 6H); ^{13}C-NMR (100 MHz, $CDCl_3$) δ 166.8, 144.3, 130.2, 129.7, 127.2,

52.2.

^{1}H and ^{13}C NMR charts were consistent with previously reported data.[2]

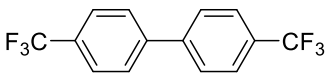

2f

2f: 33.6 mg, 58% yield, white solid; ^{1}H-NMR (400 MHz, $CDCl_3$) δ 7.75-7.69 (m, 8H); ^{13}C-NMR (100 MHz, $CDCl_3$) δ 143.3, 130.3 (q, $J_{C\text{-}F}$ = 32 Hz), 127.6, 126.0 (q, $J_{C\text{-}F}$ = 4 Hz), 124.1 (q, $J_{C\text{-}F}$ = 271 Hz); ^{19}F-NMR (376 MHz, $CDCl_3$) −62.6.

^{1}H and ^{13}C NMR charts were consistent with previously reported data.[4]

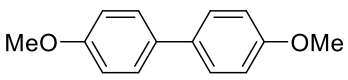

2g

2g: 21.6 mg, 50% yield, white solid; ^{1}H-NMR (400 MHz, $CDCl_3$) δ 7.49 (d, J = 8.8 Hz, 4H), 6.97 (d, J = 8.8 Hz, 4H), 3.85 (s, 6H); ^{13}C-NMR (100 MHz, $CDCl_3$) δ 158.7, 133.5, 127.7, 114.2, 55.3.

^{1}H and ^{13}C NMR charts were consistent with previously reported data.[1]

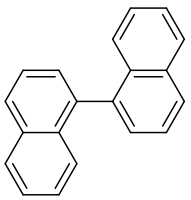

2h

2h: 29.0 mg, 57% yield, white solid; ^{1}H-NMR (400 MHz, $CDCl_3$) δ 7.97-7.94 (m, 4H), 7.60 (dd, J = 6.8Hz, 8.4 Hz, 2H), 7.51-7.45 (m, 4H), 7.39 (d, J = 8.4 Hz, 2H), 7.31-7.26 (m, 2H); ^{13}C-NMR (100 MHz, $CDCl_3$) δ 138.5, 133.5, 132.9, 128.1, 127.9, 127.8, 126.5, 126.0, 125.8, 125.4

^{1}H and ^{13}C NMR charts were consistent with previously reported data.[5]

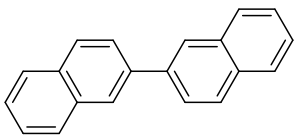

2i

2i: 41.8 mg, 82% yield, white solid; ^{1}H-NMR (400 MHz, $CDCl_3$) δ 8.19 (s, 2H), 7.98-7.94 (m, 4H), 7.91-7.89 (m, 4H), 7.55-7.51 (m, 4H); ^{13}C-NMR (100 MHz, $CDCl_3$) δ 138.4, 133.7, 132.7, 128.5, 128.2, 127.7, 126.3, 126.1, 126.0, 125.7

^{1}H and ^{13}C NMR charts were consistent with previously reported data.[1]

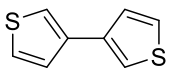

2j

2j: 17.0 mg, 51% yield, white solid; ^{1}H-NMR (400 MHz, $CDCl_3$) δ 7.39-7.33 (m, 6H); ^{13}C-NMR (100 MHz, $CDCl_3$) δ 137.2, 126.3, 126.0, 119.8.

^{1}H and ^{13}C NMR charts were consistent with previously reported data.[6]

Catalyst preparation

Cu-based catalysts were prepared by an incipient wetness impregnation. Copper (II) nitrate trihydrate was purchased from Fujifilm Wako. Titania (JRC-TIO-17), Al_2O_3 (JRC-ALO-8), Nb_2O_5 (JRC-NBO-2), and m-ZrO_2 (JRC-ZRO-3) were provided by the Catalysis Society of Japan. Amorphous ZrO_2 (am-ZrO_2, NND) was provided by Daiichi Kigenso Kagaku Kogyo. These materials were used as received. The metal oxide was impregnated with an aqueous solution of Cu nitrate. Except for CuO/am-ZrO_2, the obtained materials were dried at 110 °C for 12 h, and then calcined at 500 °C for 3 h. For CuO/am-ZrO_2, the impregnated am-ZrO_2 was dried at 110 °C for 12 h, and then calcined at 350 °C for 3 h. As a reference, we used a commercial CuO as received (Fujifilm Wako). The Cu loading of prepared catalysts was 1 mmol g_{cat}^{-1}, as listed in **Table S1**.

Table S1 Information of Cu-based catalysts.

Sample	Raw support material	Calcination temperature [°C]	Cu loading [a] [mmol g_{cat}^{-1}]
CuO/TiO_2	TiO_2	500	0.99
CuO/Al_2O_3	Al_2O_3	500	1.0
CuO/Nb_2O_5	Nb_2O_5	500	1.0
CuO/m-ZrO_2	m-ZrO_2	500	0.98
CuO/t-ZrO_2	am-ZrO_2	500	1.2
CuO/am-ZrO_2	am-ZrO_2	350	1.1

a Measured by XRF.

Characterization of catalysts

X-ray diffraction (XRD). The X-ray diffraction of the crystal structure was conducted using a Rigaku Ultima IV diffractometer. A glass plate was utilized to hold the sample powder, which was then placed within the diffractometer. The X-ray source utilized was Cu Kα, with an acceleration voltage of 40 kV and a current of 20 mA.

Synchrotron X-ray diffraction (SXRD). Synchrotron X-ray diffraction (XRD) and PDF data were collected at the BL13XU beamline with Lambda 750 K detectors in SPring-8, with the approved number of 2023A1042. The wavelength was 0.206684 Å. The powder sample was packed into a quartz glass capillary of 0.3 mm. Synchrotron powder diffraction data were converted to PDF data using the xPDF. [7]

X-ray fluorescence (XRF). The determination of Cu loading in the catalyst was carried out via XRF analysis using PANalytical Epsilon 1 instrumentation. Prior to the measurements, the Cu-containing sample was mixed with an internal standard of 99.8% pure NiO (Aldrich). The mixing ratio of the catalyst to NiO was 50wt%. The acquired data was analyzed using the fundamental parameter method,

employing Omnian software (PANalytical).

Temperature programmed reduction by H_2 (H_2-TPR). The H_2-TPR measurements were performed using a BELCAT II (MicrotracBEL) with a thermal conductivity detector. As a pretreatment, 0.1 g of the sample was heated at 300 °C for 120 minutes under an Ar flow (30 sccm). After cooling the sample to 50 °C, the introducing gas was changed from Ar to 5% H_2/Ar (30 sccm). The heating rate was set to 5.0 °C min^{-1}. For measuring the reduction peak of CuO, 0.1 g of CuO powder (Fujifilm Wako) was physically mixed with 0.9 g of SiO_2 powder (Fujifilm Wako) using a mortar, and 0.05 g of this mixture was used.

Scanning transmission electron microscopy (STEM). The particle morphology was investigated by an ultra-high resolution scanning transmission electron microscope (JEOL JEM-ARM200F) equipped with a spherical aberration corrector for a STEM probe. The sample was dispersed in ethanol (Wako, purity > 99.5%) and the suspension was dropped onto a carbon-coated molybdenum grid (Ohken shoji Co., NP-M15) to deposit the particles on the microgrid film of the grid. Elemental maps of Cu and Zr were recorded using an energy dispersive X-ray (EDX) detector.

X-ray absorption spectroscopy (XAS). Using X-ray absorption spectroscopy (XAS) at the BL14B2 beamline at SPring-8, the Cu K-edge XANES (X-ray absorption near edge structure) was measured. XAS data were collected in the quick mode. The Si (3 1 1) monochromator continuously moved from 25.415° to 22.05° over 313 s for the Cu K-edge. Spectra were collected in the transmission mode using ion chambers filled with an Ar/N_2 mixture on pressed pellets of the samples. The samples and BN were mixed using a mortar and pestle and pressed into a thin disk using a 10 mm die set. Spectra were corrected and normalized using Athena and Artemis. [8] The radial structure function (RSF) was obtained by Fourier transformation of the k^3-weighted experimental $\chi(k)$ function (k = 30-110 nm^{-1}) into the R space. Theoretical phase-shift and amplitude functions were calculated with the FEFF6 program.

X-ray photoelectron microscopy (XPS). The oxidation state of Zr, O, and Cu in the as-prepared samples was determined by XPS measurements using a JEOL JPS-9200 instrument with a Mg-Kα radiation source. The binding energy was referenced to the O 1s peak (530.0 eV).

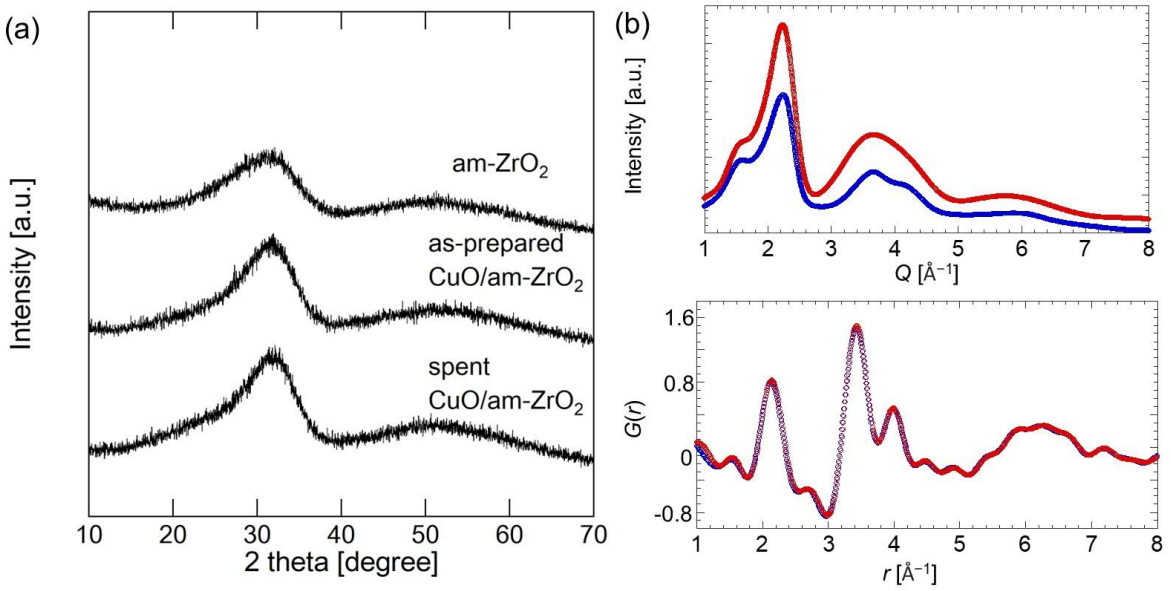

Figure S1 (a) Powder XRD patterns of am-ZrO_2 and CuO/am-ZrO_2. (b) synchrotron XRD diffraction (upper) and corresponding pair distribution function (bottom). blue: as prepared CuO/am-ZrO_2, red: spent CuO/am-ZrO_2.

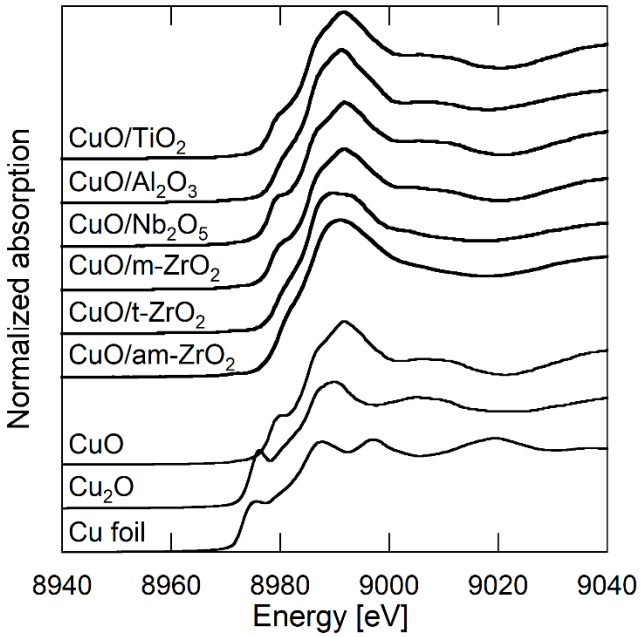

Figure S2 Cu-K edge XANES spectra of the Cu-based catalysts, CuO, Cu_2O, and Cu foil. Reproduced permission from ref. 9. Copyright 2023 The Royal Society of Chemistry.

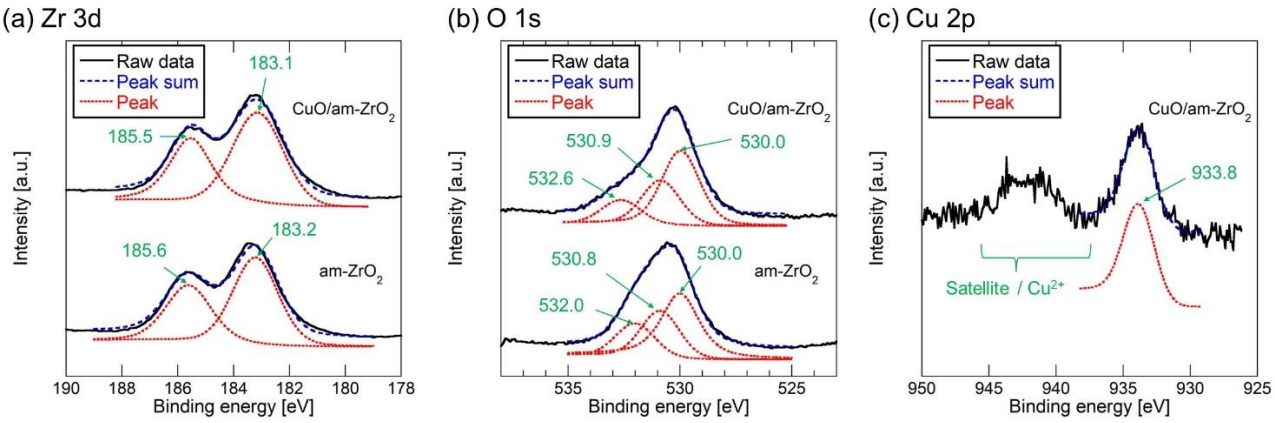

Figure S3 XPS spectra of (a) Zr 3d, (b) O 1s, and (c) Cu 2p for CuO/am-ZrO_2 and am-ZrO_2.

Figure S3 shows the XPS spectra for CuO/am-ZrO_2 and am-ZrO_2. In the Zr 3d XPS spectra of CuO/am-ZrO_2 and am-ZrO_2, peaks attributed to Zr^{4+} are observed at $3d_{5/2}$ (183.1-183.2 eV) and $3d_{3/2}$ (185.5-185.6 eV). These two peaks are known to be separated by 2.4 eV and have a peak area ratio of 1.5.[10] The O 1s XPS spectra can be deconvoluted into three peaks: the peak at 530.0 eV corresponds to lattice Zr-O bonds,[11] the peak around 531 eV is attributed to oxygen vacancies,[11] and the peak near 532 eV is due to surface hydroxyl groups.[12] Therefore, we concluded that both CuO/am-ZrO_2 and am-ZrO_2 contained oxygen vacancies. Furthermore, the Cu 2p XPS spectrum of CuO/am-ZrO_2 shows a $2p_{3/2}$ peak at 933.8 eV and satellite peaks in the range of 940-945 eV, both of which are characteristic of Cu^{2+}.

Table S2 Parameters calculated by fitting the EXAFS signals of CuO and the prepared Cu-based catalysts shown in Fig. 2 and S1 †

Sample	Shell	CN	R / Å	σ^2 / Å^2	ΔE_0 / eV	R factor
CuO	Cu-O	4 *	1.96±0.01	0.004±0.001	3.48±1.76	0.007
	Cu-O	2 *	2.76±0.08	0.012±0.015		
	Cu-Cu	4 *	2.91±0.02	0.006±0.001		
	Cu-Cu	4 *	3.10±0.01	0.006±0.002		
CuO/am-ZrO_2						
as-prepared	Cu-O	3.5±0.4	1.94±0.01	0.006±0.001	2.82±1.37	0.014
spent	Cu-O	3.5±0.4	1.94±0.01	0.005±0.001	3.12±1.48	0.015

† Notations: R, distance; CN, coordination number; σ, Debye-Waller factor; ΔE_0, increase in the threshold energy. Confidence intervals = 68%. * Fixed to the values.

Density functional theory (DFT) calculations

DFT calculations were performed using the Perdew-Burke-Ernzerhof (PBE)[13] exchange and correlation functional and D3 correction[14] using the cp2k program package,[15] based on the computational procedures reported in our previous works.[9, 16] The Goedecker-Teter-Hutter pseudopotentials[17] and a double-ζ valence plus polarization (DZVP-MOLOPT-SR-GTH)[18] Gaussian basis set for the orbitals were employed. The cutoff associated with mapping Gaussians onto a multi-grid was 60 Ry and the planewave cutoff for the finest level of the multi-grid was 400 Ry. We employed Γ point for the *k*-point samplings of the surface. The target accuracy for the SCF (self-consistent field) convergence was 10^{-5}.

CuO/am-ZrO_2 surface. The am-ZrO_2 and CuO/t-ZrO_2 surfaces were obtained from our previous works.[9, 19] The rectangular slab consisted of $Zr_{108}O_{216}$ and the dimensions of the super cell were 16.769×16.769 Å^2 and 35.000 Å along the surface-parallel and surface-normal directions, respectively. To prepare CuO/am-ZrO_2, we replaced two Cu–O_v (oxygen vacancy) pairs in the top layer of the zirconia surfaces to maintain the neutrality of the system. We first replaced Zr atoms in the supercell with Cu atoms (**Fig. S4a**). Using the optimized structure with the lowest energy, we next replaced an O atom with O_v (**Fig. S4b**). The same computations followed and resulted in $Zr_{106}Cu_2O_{214}$ (**Fig. S4c**) and $Zr_{106}Cu_2O_{213}$ (**Fig. S4d**). The surfaces shown in **Figs. S4a, S4b, S4c,** and **S4d** correspond to Cu^{4+}, Cu^{3+}, Cu^{2+}, and Cu^{+}, respectively.[20] In the calculation of adsorption energies, $Zr_{106}Cu_2O_{214}$ (**Fig. S4c**) was employed. The geometries of the surfaces were optimized under the 3D periodic boundary condition.

The structure of am-ZrO_2 was confirmed by comparing the radial distribution function obtained from DFT calculations with that from X-ray scattering experiments.[21] The difference in the peak positions was 0.16 Å on average of all peaks. This agreement of the peak positions indicates that the simulated bulk am-ZrO_2 reproduces the experimental structure of am-ZrO_2. Additionally, the weaker adsorption of CO_2 and methanol observed in experiments[19, 22] was also reproduced using the surface model employed in this study. These previous findings indicate that the model used is sufficiently accurate to discuss the structure and adsorption strength of am-ZrO_2.

Fig. S4 shows the positions of Cu and O_v, and **Table S3** summarizes the coordination numbers and Hirshfeld charges by Hirshfeld analysis[23] using a hybrid functional (PBE + 10.5% Hartree-Fock exchange).[24] of two Cu atoms. As the number of O_v increases, the coordination numbers and Hirshfeld charges of two Cu atoms decrease, which indicates Cu atoms are reduced.

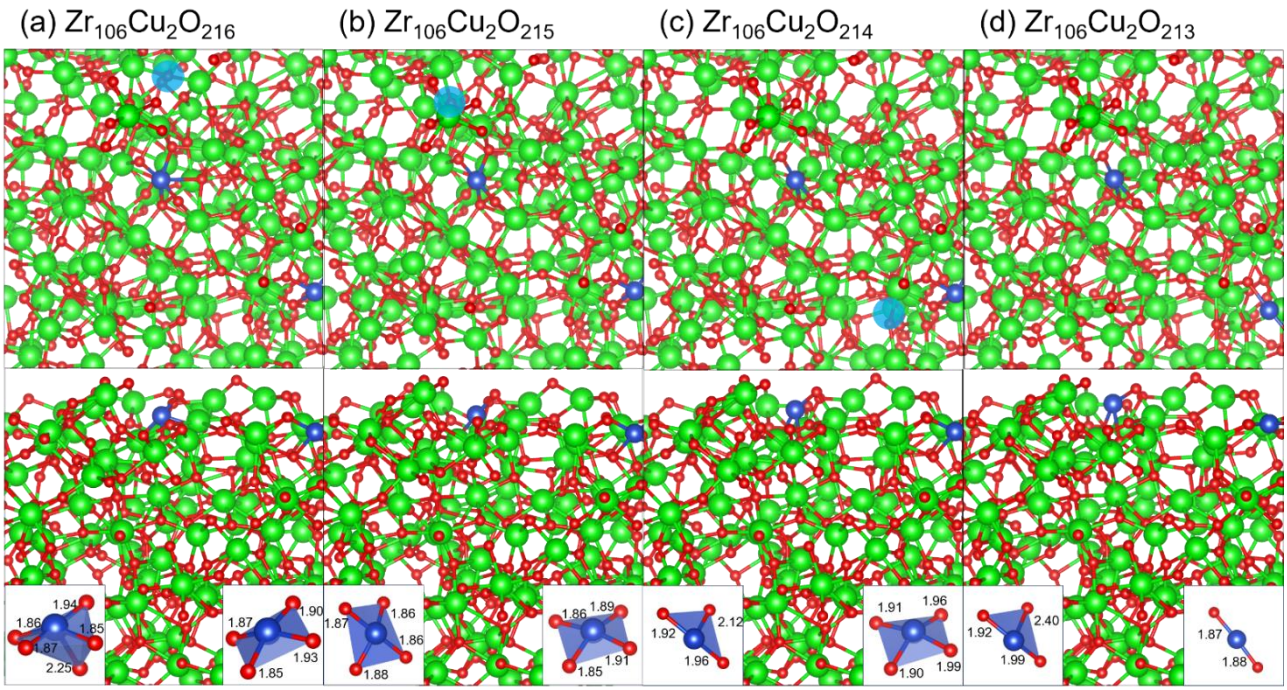

Figure S4 Top and side views of the optimized $CuZrO_x$ surfaces. The positions of oxygen vacancies are marked by blue circles. The insets show the snapshots of the CuO clusters, and the bond lengths (Å) are also shown. Color code: green: Zr, red: O, and blue: Cu. The figures were made by VESTA.[25]

Table S3 The coordination numbers (n) and Hirschfeld charges (q) of Cu atoms.

	(a) $Cu_2Zr_{106}O_{216}$	(b) $Cu_2Zr_{106}O_{215}$	(c) $Cu_2Zr_{106}O_{214}$	(d) $Cu_2Zr_{106}O_{213}$
n (Cu1)	5	4	3	3
n (Cu2)	4	4	4	2
q (Cu1)	0.659	0.640	0.484	0.370
q (Cu2)	0.643	0.637	0.605	0.387

Free energy of formation. Using the calculated energies for the surfaces shown in **Fig. S4**, we estimated the free energy difference of formation from the Cu^{4+} reference state given by previous reports.[20, 26]

$$\Delta G = G(\mathrm{Cu}^{4-n}) - G(\mathrm{Cu}^{4+}) + n\mu_{\mathrm{O}}.$$

Here, $G(\mathrm{Cu}^{m})$ denotes the free energy for the Cu^{m} state. The entropic contributions are neglected in this study and approximated by the energies by DFT calculations. The chemical potential of oxygen at a given temperature T and pressure p is defined[20, 26]

$$\mu_{\mathrm{O}} = \mu_{\mathrm{O}}(T, p^{\mathrm{o}}) + \frac{k_{\mathrm{B}}T}{2}\ln\left(\frac{p}{p^{\mathrm{o}}}\right),$$

where k_{B} is the Boltzmann constant and p^{o} is the standard pressure of oxygen ($p^{\mathrm{o}} = 1$ atm). The

energy of oxygen calculated by DFT ($E_{O_2/2}$) was taken as a zero-reference state for μ_O. Since the reaction underwent at 50 ˚C in our experiment, we approximately assumed $\mu_O(T, p^o) = -0.27$ eV (300 K) for the chemical potential of oxygen.[26]

Fig. S5 shows the phase diagram of the CuO/am-ZrO_2 surface by plotting the free energy difference of formation as a function of chemical potential of oxygen. In the O-rich limit (high pressure of oxygen and high μ_O), the energy of Cu^{3+} is lower and the Cu^{3+} state is preferred. Notably, compared to the phase diagram of the CuO/t-ZrO_2 surface,[9] the formation free energy of Cu^{3+} is lower in a wide range of the chemical potential of O at the CuO/am-ZrO_2 surface. This indicates the stability of Cu^{3+}, and agrees with the proposed reaction mechanism.[9] The oxidation of Cu^{2+} to Cu^{3+} occurs by O_2 in air. The high oxidation state of Cu is in line with the shorter Cu-O bond lengths at the CuO/am-ZrO_2 surface (1.90–1.99 Å for the [CuO_4] cluster in the Cu^{2+} state) in **Fig. S4** than at the CuO/t-ZrO_2 surface (1.94–2.00 Å).[9] Because the Zr-O bonds at the am-ZrO_2 surface are stronger than at the t-ZrO_2 surface,[16] it is suggested that Cu-O bonds are also stronger in the more rigid zirconia surface.

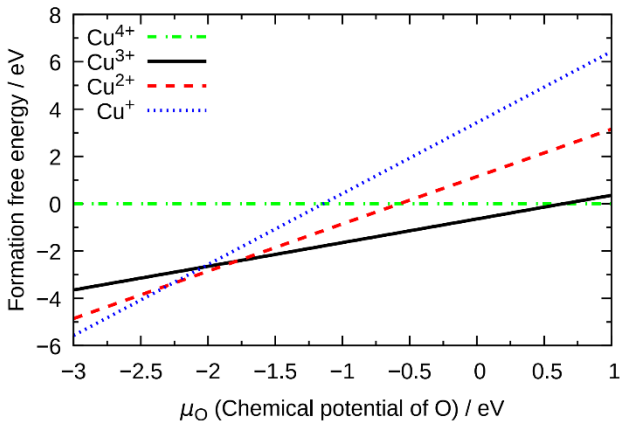

Figure S5 Formation free energy on the CuO/am-ZrO_2 surfaces as a function of the chemical potential of O atom for Cu^{4+}, Cu^{3+}, Cu^{2+}, and Cu^{+} oxidation states at the reaction temperature.

Adsorption energy. The adsorption energy was calculated using the equation,

$$E_{ads} = E_{substrate+adsorbate} - E_{substrate} - E_{adsorbate},$$

where $E_{substrate+adsorbate}$, $E_{substrate}$, and $E_{adsorbate}$ are the energies of the substrate and adsorbate, substrate, and adsorbate, respectively. The adsorbates were $PhB(OH)_2$ (phenylboronic acid) and $PhB(OH)_2$ + C_6H_6 (benzene). The adsorbates were placed on the optimized surfaces shown in **Fig. S4c** to form four Cu-O bonds (Bonds with bond lengths of 2.6 Å or less were considered bonded.).

References

1. G. Cheng and M. Luo, *Eur. J. Org. Chem.,* 2011, 2519.
2. T. Yurino, Y. Ueda, Y. Shimizu, S. Tanaka, H. Nishiyama, H. Tsurugi, K. Sato and K. Mashima, *Angew. Chem. Int. Ed.,* 2015, **54**, 14437.
3. J. Lakshmidevi, R. M. Appa, B. R. Naidu, S. S. Prasad, L. S. Sarma and K. Venkateswarlu, *Chem. Commun.*, 2018, **54**, 12333.
4. S. Bajo, G. Laidlaw, A. R. Kennedy, S. Sproules and D. J. Nelson, *Organometallics,* 2017*,* **36***,* 1662.
5. S. Ostrowska, S. Rogalski, J. Lorkowski, J. Walkowiak and C. Pietraszuk, *Synlett,* 2018*,* **29***,* 1735.
6. P. B. Dzhevakov, M. A. Topchiy, D. A. Zharkova, O. S. Morozov, A. F. Asachenko and M. S. Nechaev, *Adv. Synth. Catal.,* 2016, **358**, 977.
7. X. Yang, P. Juhas, C. L. Farrow and S. J. L. Billinge, https://arxiv.org/abs/1402.3163.
8. B. Ravel and M. Newville, *J. Synchrotron Radiat.*, 2005, **12**, 537.
9. M. Kondo, T. Joutsuka, K. Fujiwara, T. Honma, M. Nishijima, and S. Tada, *Catal. Sci. Technol.*, 2023, **13**, 2247.
10. (*a*) P. Lackner, Z. Zou, S. Mayr, U. Diebold and M. Schmid, *Phys. Chem. Chem. Phys.*, 2019, **21**, 17613; (*b*) C. Morant, J.M. Sanz, L. Galán, L. Soriano and F. Rueda, *Surf. Sci.*, 1989, **218**, 331.
11. F. Sha, C. Tang, S. Tang, Q. Wang, Z. Han, J. Wang and C. Li, *J. Catal.*, 2021, **404**, 383
12. J. A. Navio, M. C. Hidalgo, G. Colon, S. G. Botta and M. I. Litter, Langmuir 2001, **17**, 202.
13. J. P. Perdew, K. Burke, and M. Ernzerhof, *Phys. Rev. Lett.*, 1996, **77**, 3865.
14. S. Grimme, J. Antony, S. Ehrlich, and H. Krieg, *J. Chem. Phys*., 2010, **132**, 154104.
15. T. D. Kühne , M. Iannuzzi , M. Del Ben , V. V. Rybkin and P. Seewald, *et al.*, *J. Chem. Phys*., 2020, **152**, 194103.
16. S. Tada, N. Ochiai, H. Kinoshita, M. Yoshida, N. Shimada, T. Joutsuka, M. Nishijima, T. Honma, N. Yamauchi, Y. Kobayashi, and K. Iyoki, *ACS Catal*., 2022, **12**, 7748.
17. (a) S. Goedecker, M. Teter, and J. Hutter, *Phys. Rev. B,* 1996, **54**, 1703; (b) C. Hartwigsen, S. Goedecker, and J. Hutter, *Phys. Rev. B,* 1998, **58**, 3641.
18. J. VandeVondele and J. Hutter, *J. Chem. Phys*., 2007, **127**, 114105.
19. T. Joutsuka and S. Tada, *J. Phys. Chem. C,* 2023, **127**, 6998.
20. J. S. Elias, N. Artrith, M. Bugnet, L. Giordano, G. A. Botton, A. M. Kolpak, and Y. Shao-Horn, *ACS Catal*., 2016, **6**, 1675.
21. K. Sugiyama, Y. Waseda, S. Kudo, *ISIJ. Int.,* 1991, **31**, 1362.
22. S. Tada, A. Katagiri, K. Kiyota, T. Honma, H. Kamei, A. Nariyuki, S. Uchida and S. Satokawa, *J. Phys. Chem. C*, 2018, **122**, 5430.
23. F. L. Hirshfeld, *Theor. Chim. Acta,* 1977, **44**, 129.
24. (a) A. R. Elmaslmane, M. B. Watkins, and K. P. McKenna, *J. Chem. Theory Comput*., 2018, **14**, 3740; (b) T. Joutsuka, H. Yoshinari, and S. Yamauchi, *Bull. Chem. Soc. Jpn*., 2021, **94**, 106.

25. K. Momma and F. Izumi, *J. Appl. Crystallogr*., 2011, **44**, 1272.
26. K. Reuter and M. Scheffler, *Phys. Rev. B,* 2001, **65**, 035406.

NMR Charts

^{1}H-NMR (400 MHz, $CDCl_3$) chart of **2a**

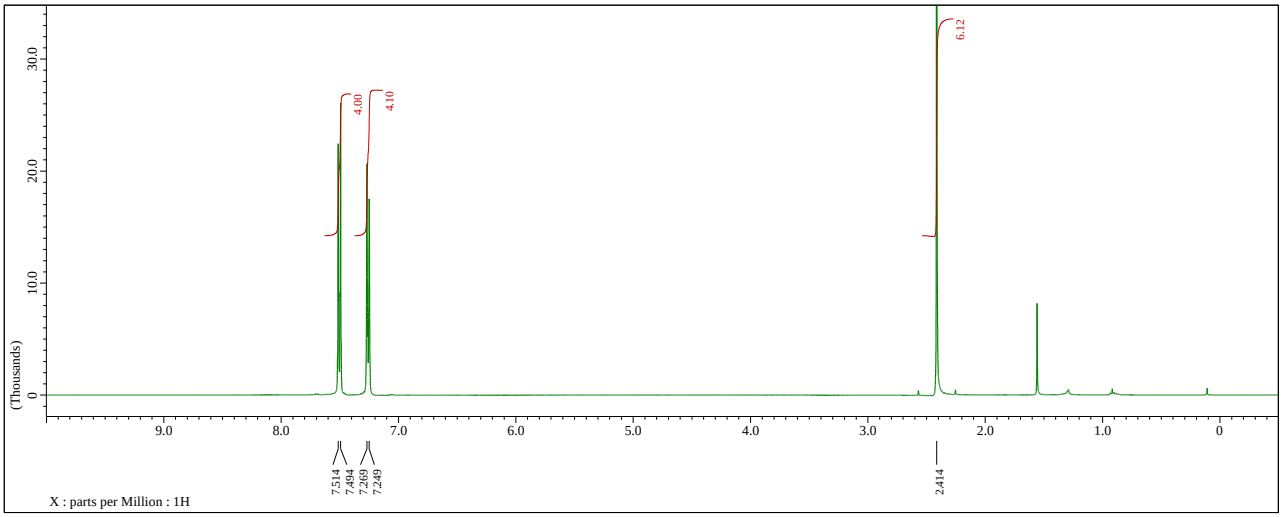

^{13}C-NMR (100 MHz, $CDCl_3$) chart of **2a**

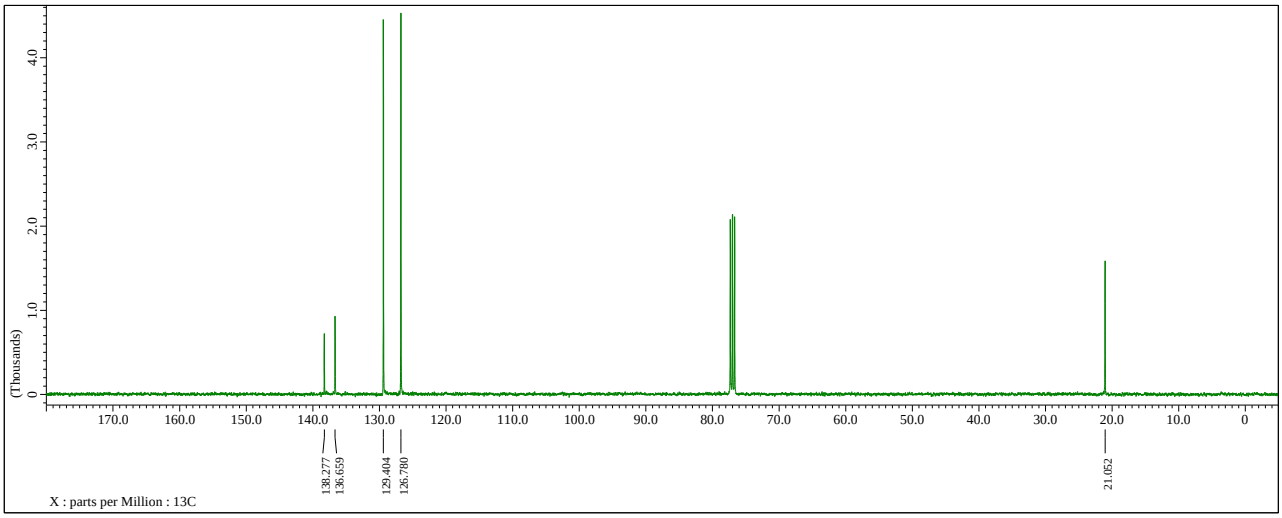

^{1}H-NMR (400 MHz, $CDCl_3$) chart of **2b**

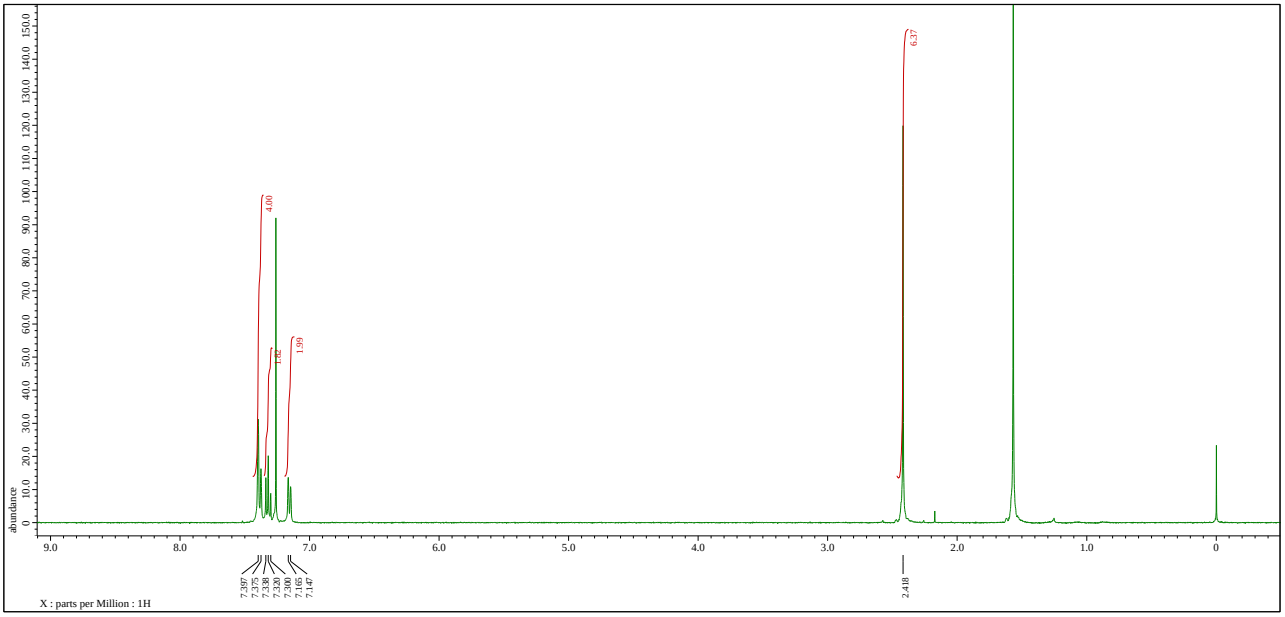

^{13}C-NMR (100 MHz, $CDCl_3$) chart of **2b**

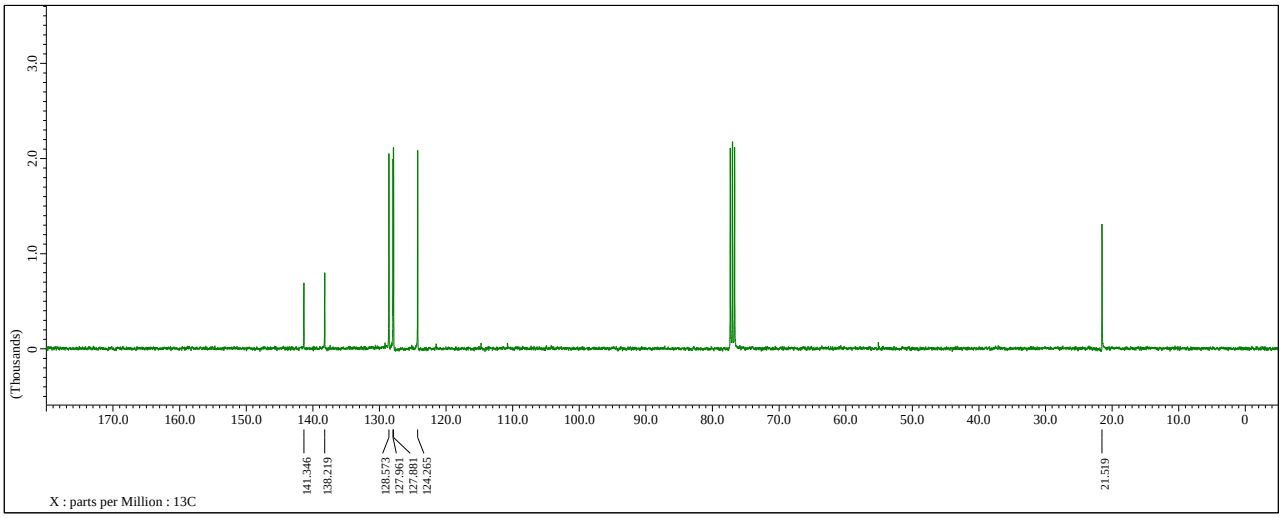

^{1}H-NMR (400 MHz, $CDCl_3$) chart of **2c**

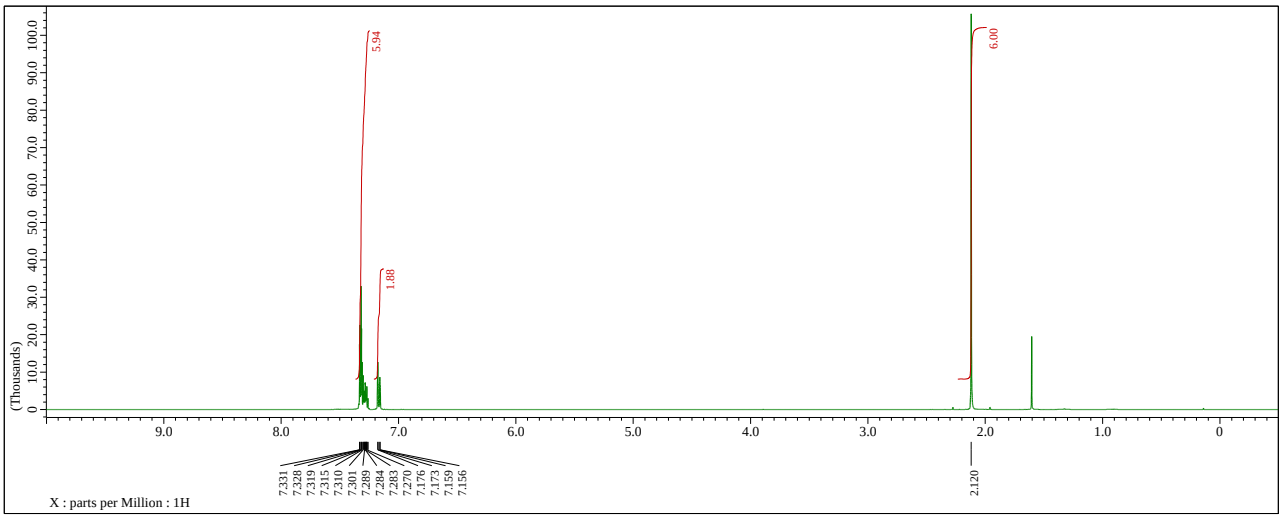

^{13}C-NMR (100 MHz, $CDCl_3$) chart of **2c**

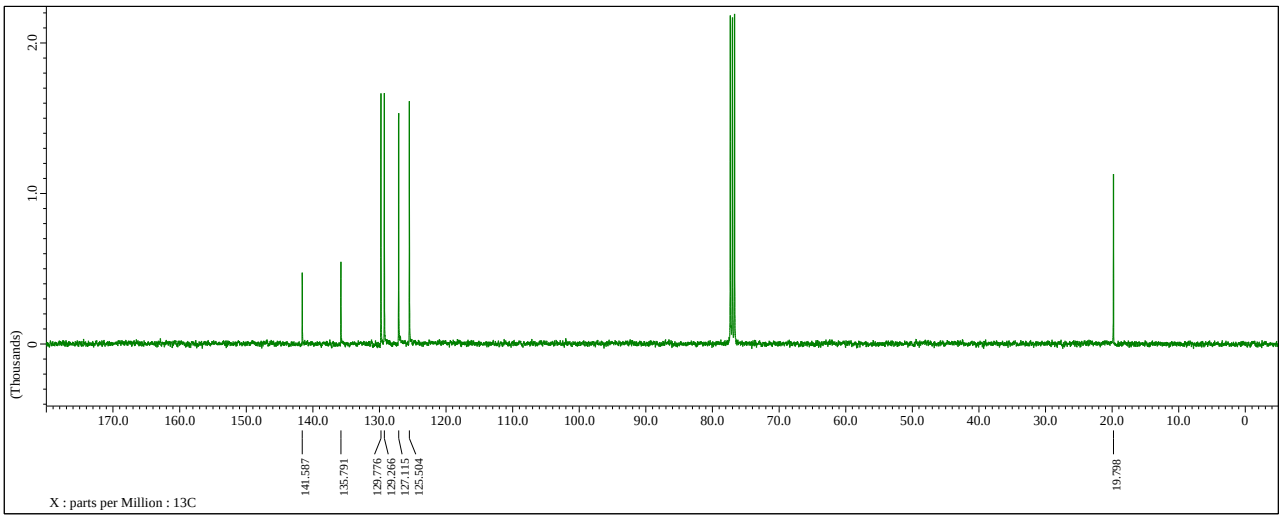

^{1}H-NMR (400 MHz, $CDCl_3$) chart of **2d**

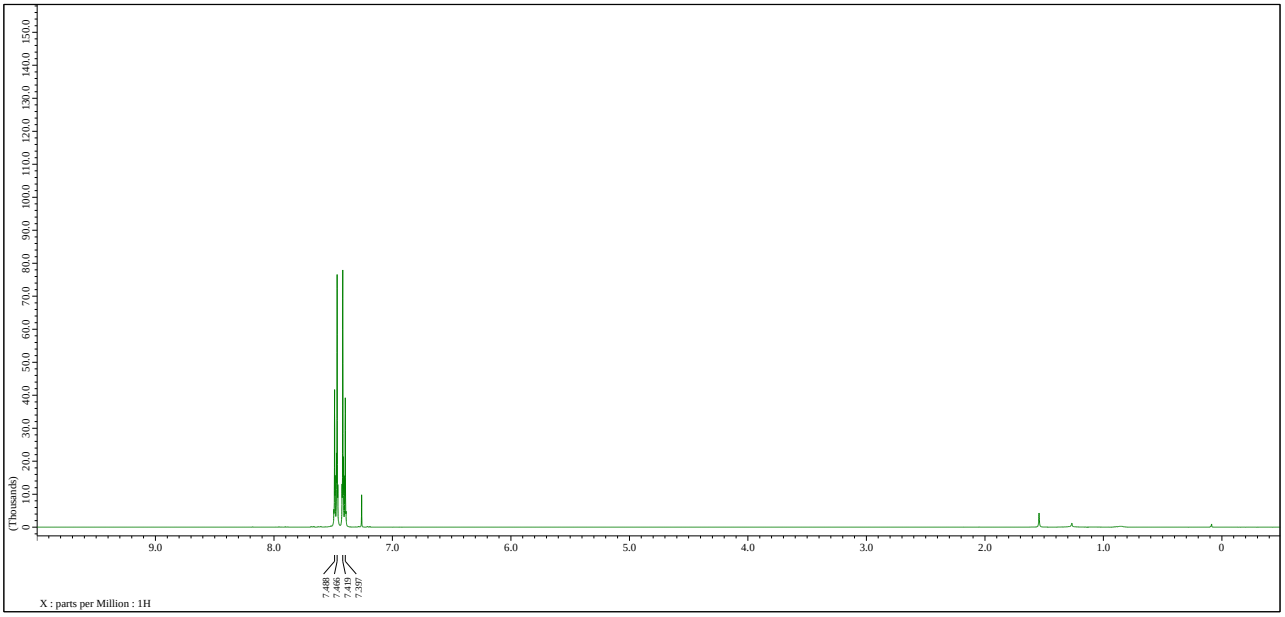

^{13}C-NMR (100 MHz, $CDCl_3$) chart of **2d**

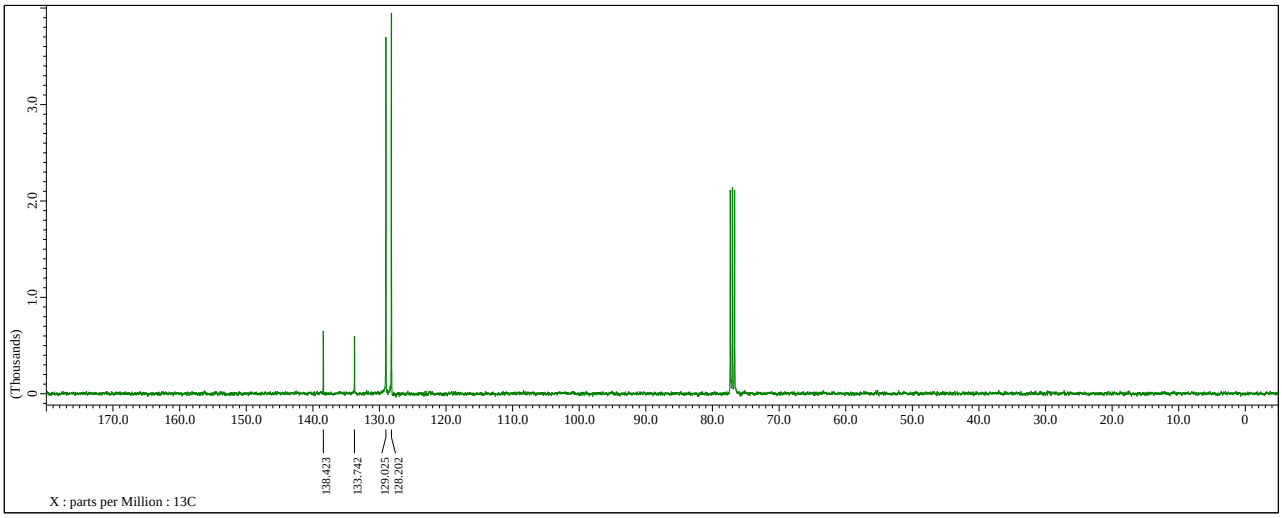

^{1}H-NMR (400 MHz, $CDCl_3$) chart of **2e**

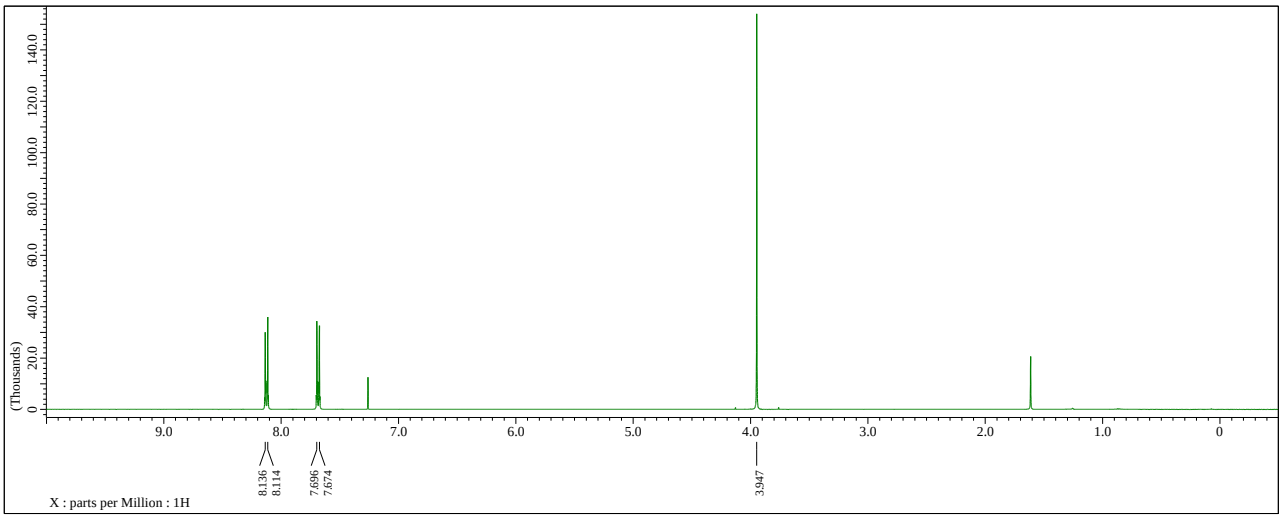

^{13}C-NMR (100 MHz, $CDCl_3$) chart of **2e**

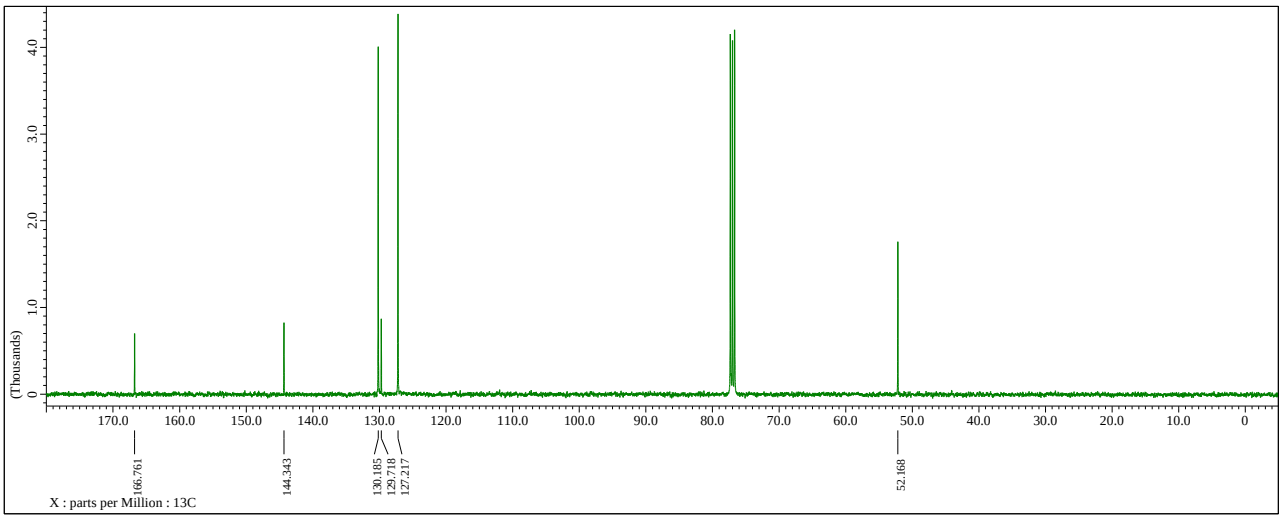

^{1}H-NMR (400 MHz, $CDCl_3$) chart of **2f**

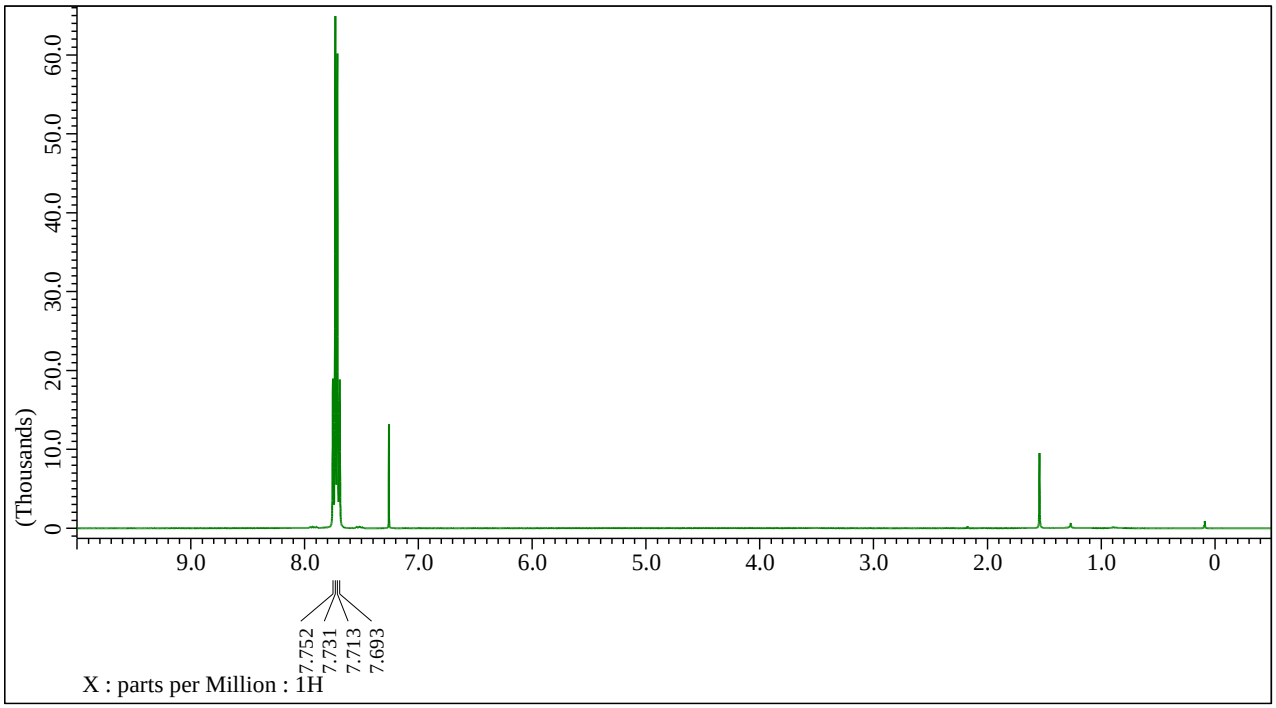

^{13}C-NMR (100 MHz, $CDCl_3$) chart of **2f**

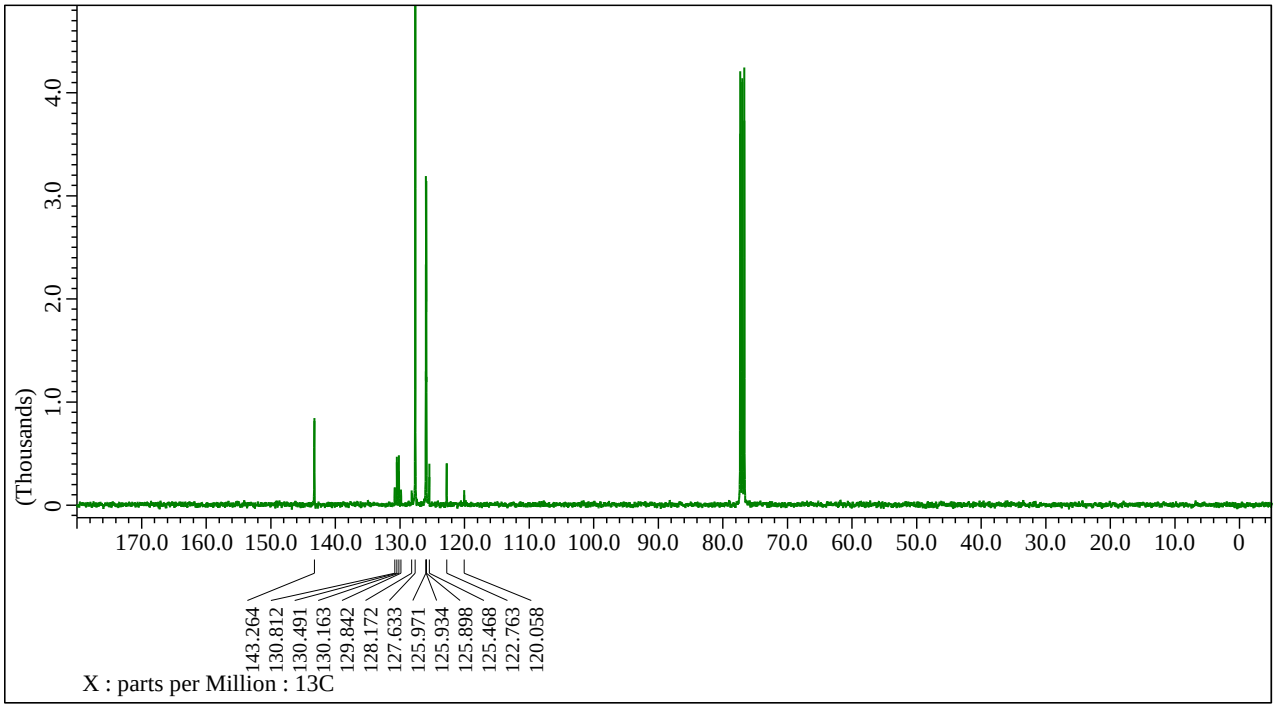

^{19}F-NMR (376 MHz, $CDCl_3$) chart of **2f**

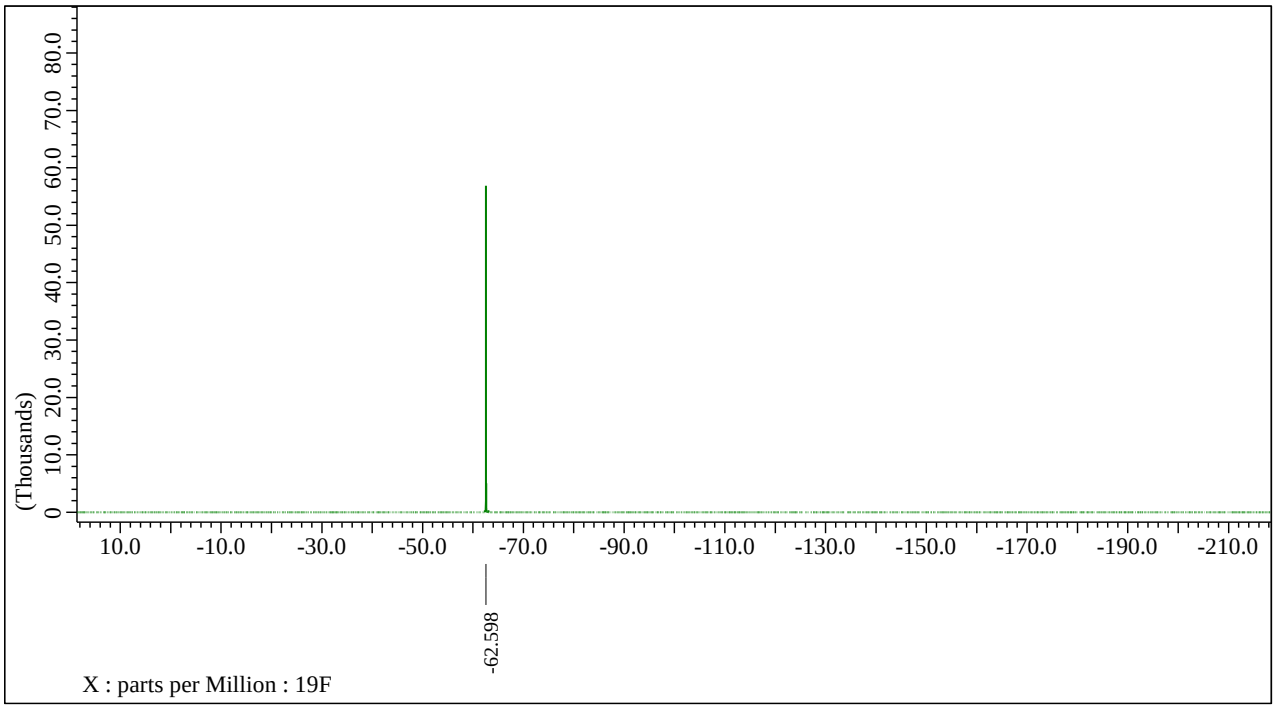

^{1}H-NMR (400 MHz, $CDCl_3$) chart of **2g**

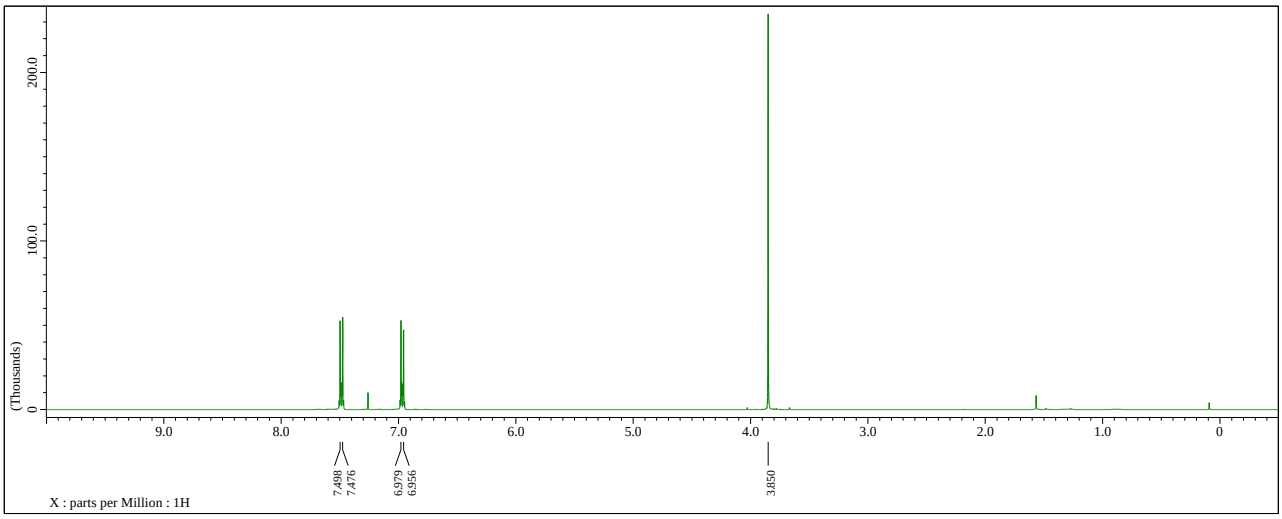

^{13}C-NMR (100 MHz, $CDCl_3$) chart of **2g**

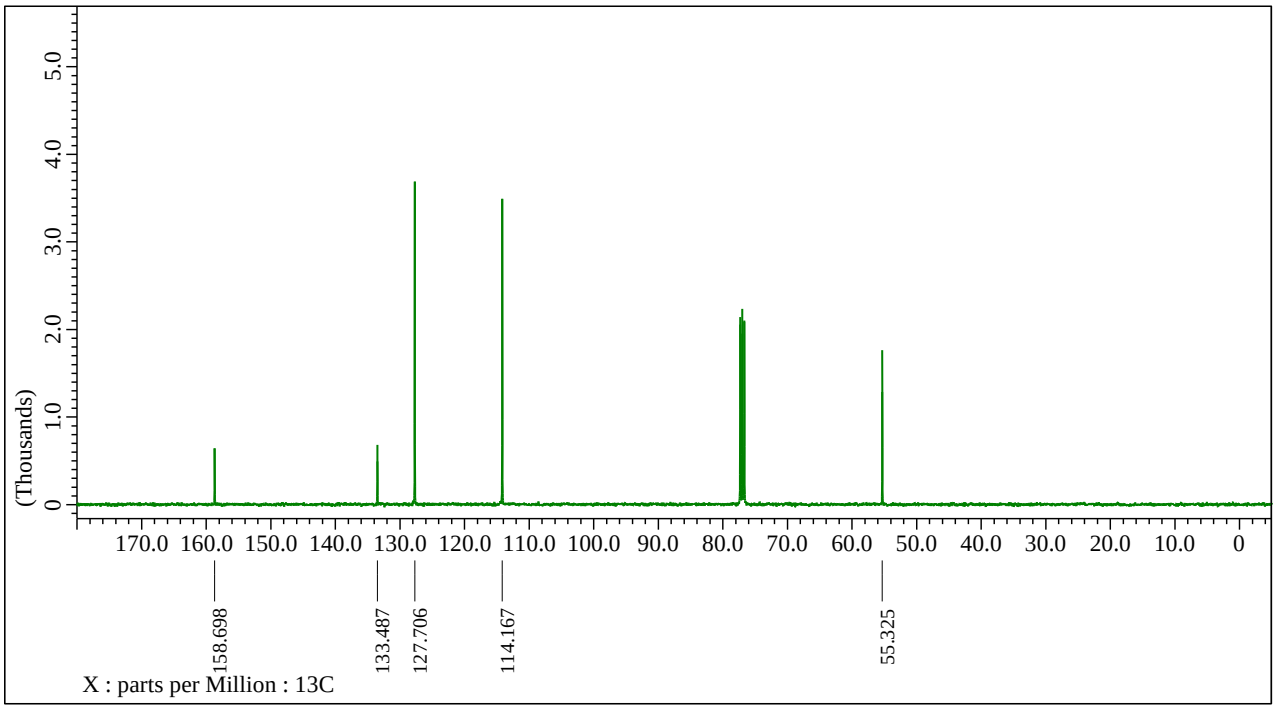

^{1}H-NMR (400 MHz, $CDCl_3$) chart of **2h**

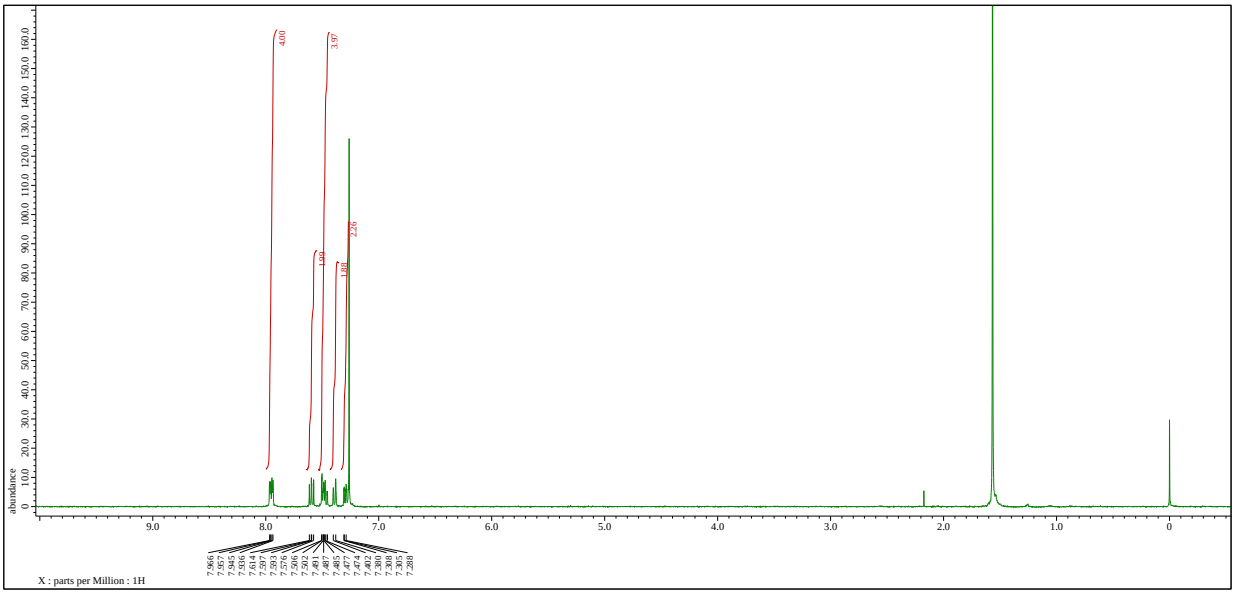

^{13}C-NMR (100 MHz, $CDCl_3$) chart of **2h**

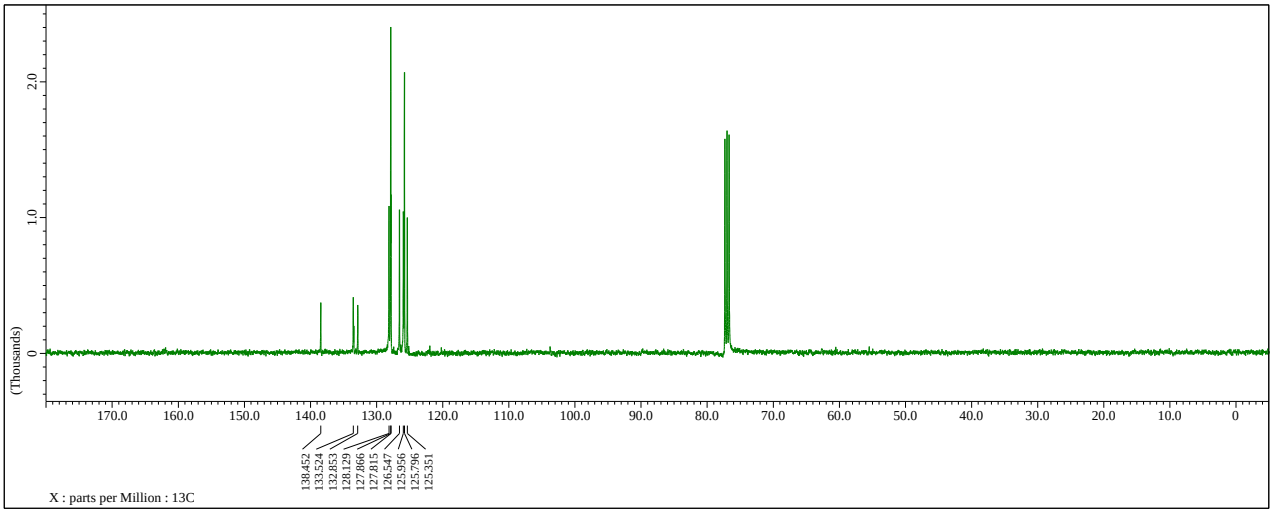

^{1}H-NMR (400 MHz, $CDCl_3$) chart of **2i**

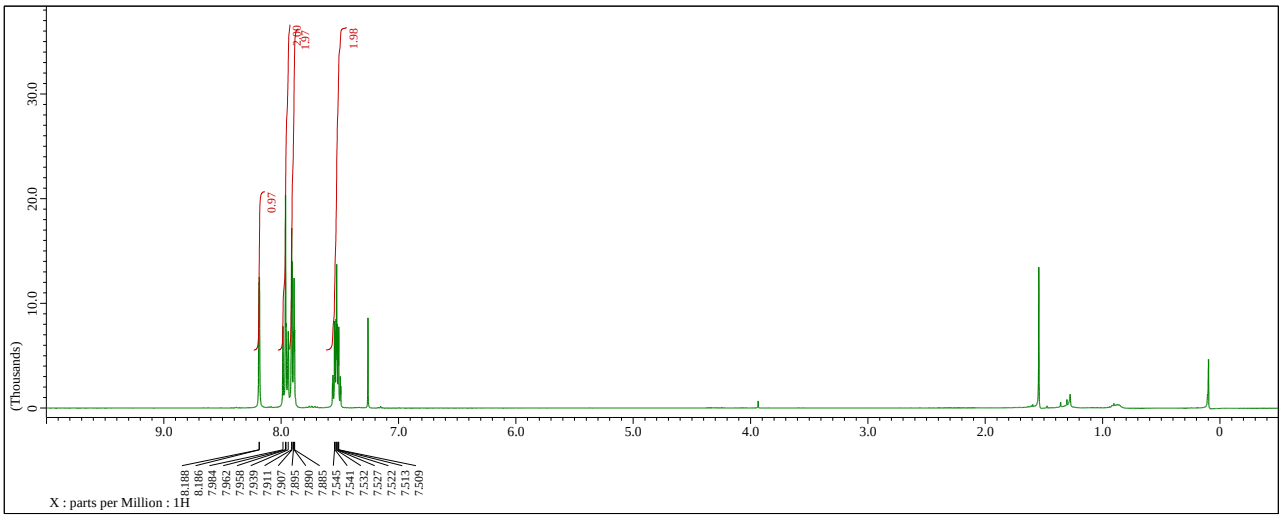

^{13}C-NMR (100 MHz, $CDCl_3$) chart of **2i**

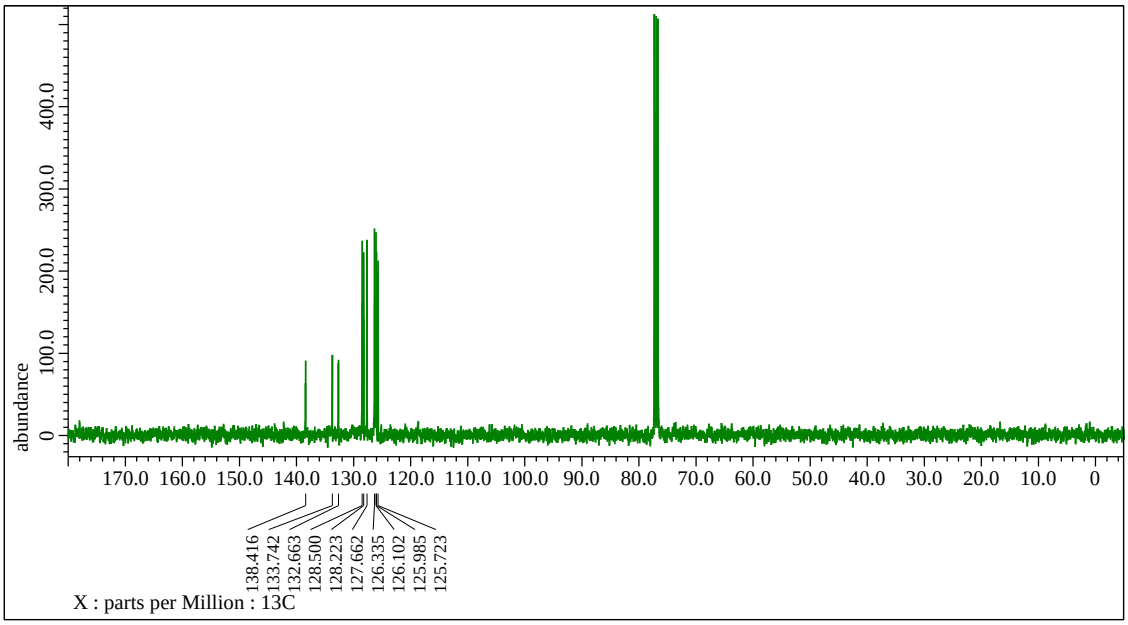

^{1}H-NMR (400 MHz, $CDCl_3$) chart of **2j**

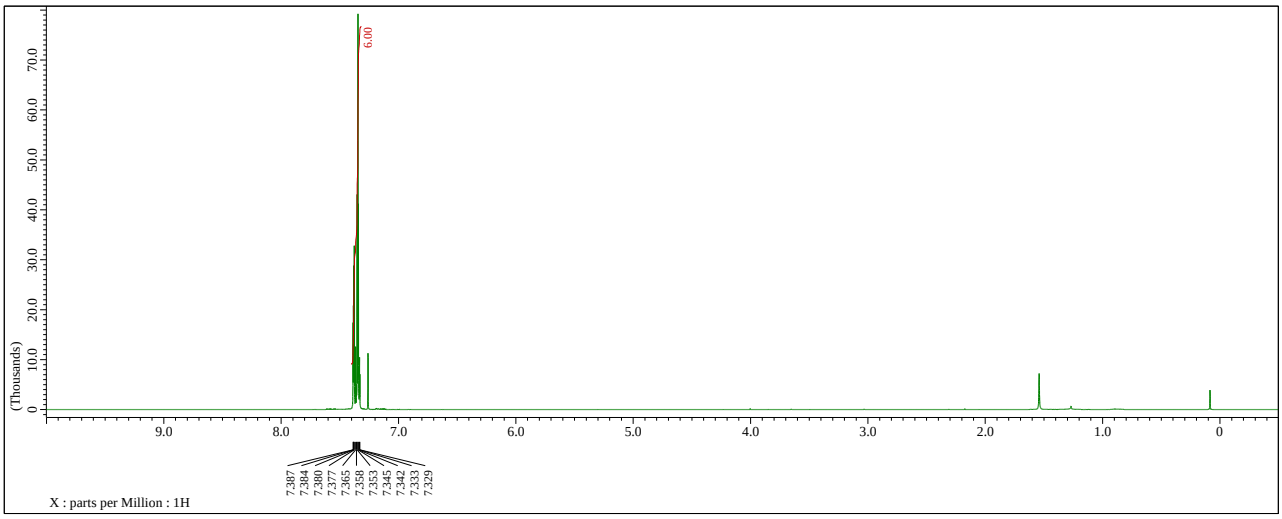

^{13}C-NMR (100 MHz, $CDCl_3$) chart of **2j**